Angewandte Chemie International Edition

Angewandte International Edition Chemie

GDCh German Chemical Society

How to cite: *Angew. Chem. Int. Ed.* **2026**, 65, e26011
doi.org/10.1002/anie.202526011

RESEARCH ARTICLE OPEN ACCESS

Extended Fused Carbazole-BODIPY, High Brightness NIR Organic Dyes

Fabien Ceugniet[1] | Valentin Ott[1] | Pascal Retailleau[2] | Yann Bretonniere[3] | Olivier Maury[3] | Manon H. E. Bousquet[4] | Lucie Sancey[5] | Nicolas Leclerc[1] | Denis Jacquemin[4,6] | Gilles Ulrich[1]

[1]Institut De Chimie et Procédés Pour L'energie, L'environnement Et La Santé (ICPEES), CNRS UMR 7515, École De Chimie Polymères, Matériaux De Strasbourg (ECPM), Strasbourg, Cedex, France | [2]Service De Cristallographie Structurale, ICSN-CNRS Université Paris-Saclay, Gif-sur-Yvette, Cedex, France | [3]LCH, UMR 5182 CNRS-ENS Lyon-Université Lyon I, France | [4]Nantes Université, CNRS, CEISAM, Nantes, France | [5]Université Grenoble Alpes, INSERM U 1209, CNRS UMR 5309, Institute For Advanced Biosciences, Grenoble, France | [6]Institut Universitaire de France (IUF), Paris, France

Correspondence: Nicolas Leclerc (leclercn@unistra.fr) | Denis Jacquemin (Denis.Jacquemin@univ-nantes.fr) | Gilles Ulrich (gulrich@unistra.fr)

Received: 24 November 2025 | **Revised:** 27 February 2026 | **Accepted:** 27 February 2026

Keywords: BODIPY | coupling | imaging | NIR dyes

ABSTRACT

Fluorescence-based bioimaging enables noninvasive visualization of molecular and cellular processes with high sensitivity and without ionizing radiation. However, conventional fluorophores emitting in the visible or near-red infrared I (NIR-I) (650–800 nm) regions suffer from limited tissue penetration and scattering. Extending fluorescence emission into the deeper NIR region represents a promising strategy to overcome these drawbacks, yet achieving high brightness and stability in organic dyes remains a major challenge. We report an original family of hetero-substituted-fused boron-dipyrromethene (BODIPY) dyes bearing carbazole and thienyl donors that exhibit record brightness and emission maxima up to 852 nm in toluene. The synthetic route combines successive Stille couplings from a 2,6-dibromo-3,5-diiodo-BODIPY precursor and an unprecedented silver(I)-mediated oxidative cyclization, affording high yields and suppressing undesired chlorination. The resulting dyes display intense absorption ($\varepsilon = 1.8–2.5 \times 10^5$ M^{-1} cm^{-1}) and exceptional fluorescence quantum yields (Φ up to 0.73). Encapsulation in silica nanoparticles (NPs) preserves their photophysical properties and enables efficient NIR-II in vivo imaging in mice, allowing tumor detection at doses as low as 0.2 nmol with tumor-to-muscle ratios > 4. These fused BODIPY derivatives rank among the brightest NIR fluorophores reported to date and open new avenues for high-contrast deep-tissue imaging and image-guided surgery.

1 | Introduction

Fluorescence-based biological imaging is a powerful approach to noninvasively visualize dynamic, functional, and molecular events in living organisms, without ionization and at low contrast agent concentration, in contrast to both nuclear imaging and magnetic resonance imaging, respectively [1]. Fluorescence imaging agents emitting in the visible and the close near-red infrared I (NIR-I, 650–800 nm) regions are now well developed for imaging in living cells or tissues. However, a high in vivo resolution with these imaging agents is difficult to achieve due to scattering and interference by the tissue. Using fluorescent imaging agents operating deeper in the NIR-I (800–950 nm) or NIR-II (1000–1700 nm) regions is one of the strategies allowing overcoming the above-mentioned hurdles [2]. The deep penetration of light in NIR-II, concomitantly with highly reduced diffusion and absence of competitive endogenic absorption or emission, make such agents highly desirable for biological labeling, disease detection, and real-time imaging as image-guided surgery [3]. The most important feature for fluorescence-based imaging is the brightness (B), the product of the molar absorptivity (ε) and fluorescence quantum yield (Φ). In addition, such dyes can be attractive for

applications in optoelectronics, for example, in light transparent organic photovoltaic [4, 5] and NIR photodiodes/photodetectors [6].

The potential of NIR-II fluorescence bioimaging has been demonstrated using both single-walled nanotubes and inorganic nanoparticles (NPs), yet their poor Φ have prompted the development of more efficient organic fluorophores [7]. To push the emission of organic fluorophores in the NIR-II region, strategies such as extended π-conjugation, structural rigidification, insertion of electron-donating groups leading to donor–acceptor–donor (D–A–D) architectures, and the use of polymethine cores with intrinsically high B have been explored [2, 3, 8, 9]. However, NIR-II dyes often suffer from chemical instability in biological media: their low-lying LUMO makes them sensitive to nucleophilic attack while their high-lying HOMO increases susceptibility to oxidation or electrophilic attack. In addition, according to the *energy gap law*, dyes with narrow bandgaps typically exhibit low B due to the inherent enhancement of nonradiative processes (deformation, vibrational coupling, low-lying charge transfer states, intersystem coupling…) [10]. As a result, the development of such efficient fluorophores remains challenging. The few available imaging agents, often based on xanthenes [11] or polymethines [12–14], still suffer from photobleaching, low Φ, and/or limited water solubility [15–17].

In this context, NIR-I fluorophores combining an off-peak tail emission above 1000 nm and a high B offer a promising alternative. Additionally, such compounds are compatible with conventional microscopy and flow cytometry systems due to their NIR-I emission, while remaining detectable when using NIR-II cameras. This has been demonstrated in the FDA-approved Indocyanine Green (ICG) dye [18] and Methylene blue [19].

Amongst the various NIR imaging agents [20–24], compact organic fluorophores are particularly attractive due to their minimal interaction with living organisms and easy connection to bioligands (peptide, antibody, sugars…), making them excellent candidates for clinical imaging reagents. In this regard, Boron-dipyrromethene (BODIPY) dyes stand out for their excellent biocompatibility and tunable photophysical properties [25]. Recent studies have shown that rational design can redshift BODIPY emission into the NIR while retaining significant brightness. Vinyl-bridged BODIPY oligomers, for instance, exhibit emission maxima (λ_{em}) spanning from 720 to 1136 nm, yet with moderate B [26]. NIR-II emitting aza-BODIPY dyes were developed by introducing strong electron-donating groups at several positions of the aza-BODIPY core or its gallium analog [27, 28], with some derivatives optimized for aqueous solubility [29, 30]. A family of NIR II-emitting dyes with high NIR emission potential was reported through a cyanine-BODIPY hybridization strategy [31]. Despite these advances, further progresses are needed for enhancing both the depth of NIR emission and overall brightness.

Here, we present an innovative series of hetero-substituted-fused BODIPY dyes featuring outstanding brightness with emissions maximum up to 852 nm in toluene. Importantly, these compounds rank amongst the brightest reported dyes in this spectral domain. We report their original synthesis (including a new set of conditions for oxidative cyclization), along with their theoretical and optical properties characterizations. Additionally, to demonstrate their potential as NIR fluorescent probes, one of these new dyes was encapsulated into polymeric NPs, and promising preliminary imaging results are presented.

1.1 | Design and Synthesis

Our previous work on hetero-substituted-fused BODIPY paved the way for synthesizing BODIPY with redshifted emission [32]. When five-member ring substituents (thienyls) are introduced on the 3,5-positions of the BODIPY and 6-member rings (anisoles) on its 2,6-positions (Figure 1, left), the resulting fused aromatic core showed a perfectly planar structure in both its ground and the excited states according to ab initio calculations. This fully rigid structure allows an excellent delocalization in the π-system while limiting detrimental nonradiative deexcitations. However, the emission of this compound is insufficiently redshifted, and its Φ is too small for biological imaging, likely due to the free rotations of methoxy groups (rotor effect). To address these issues, fused carbazole moieties are selected here as electron donors at the 2,6-positions of the BODIPY. The additional thiophene-based aromatic rings at the 3,5-positions, are designed to induce a bathochromic shift of both the absorption and the emission while maintaining the planarity of the whole molecule, thanks to the heteroatoms, therefore hampering nonradiative deexcitation pathways.

The results obtained for **1a** led us to extend this approach, aiming at further redshifting the emission of our compounds by extending the length of the π-conjugated system, this time, using the thienyl substituents (**1b,c**, Scheme 1). Finally, in order to investigate the donor effect of carbazole units, the orientation with respect to the BODIPY plane can be reversed (**1d**).

2 | Results and Discussion

The synthesis of the fused BODIPY **1a–d** is carried out following our reported strategy with a stepwise introduction of the substituents [27, 33], see Scheme 1. First, the thiophene-based substituents are regioselectively introduced at the 3,5-positions of the 2,6-dibromo-3,5-diodo BODIPY **2** by a Stille coupling reaction in 50%–64% yields (Scheme S1). A second Stille cross-coupling is employed to attach the selected carbazole substituents at the 2,6-positions in good yields (71%–86%). As reported by Müllen et al., using the common mild oxidant $FeCl_3$ for the oxidative cyclization produces the desired compounds, yet, in some cases, leads to inseparable parasitic chlorinated by-products [34]. To circumvent this issue, we propose a new synthetic method using $AgBF_4$ as an oxidant, which allows obtaining the pure compounds **1a-d** in 49%–81% yields. All molecules are characterized by NMR and HRMS spectroscopies.

The absorption and emission spectra of all final compounds and intermediates measured in dichloromethane (DCM) and the associated data can be found in the Supporting Information. As presented in Figure 2a–d, all the fused compounds **1a-d** exhibit intense absorption and emission in the NIR region with exceptional quantum yields for this spectral range in both toluene and DCM (Table 1). Compound **1a** has an emission maximum at 788 nm in toluene with an excellent Φ of 0.73.

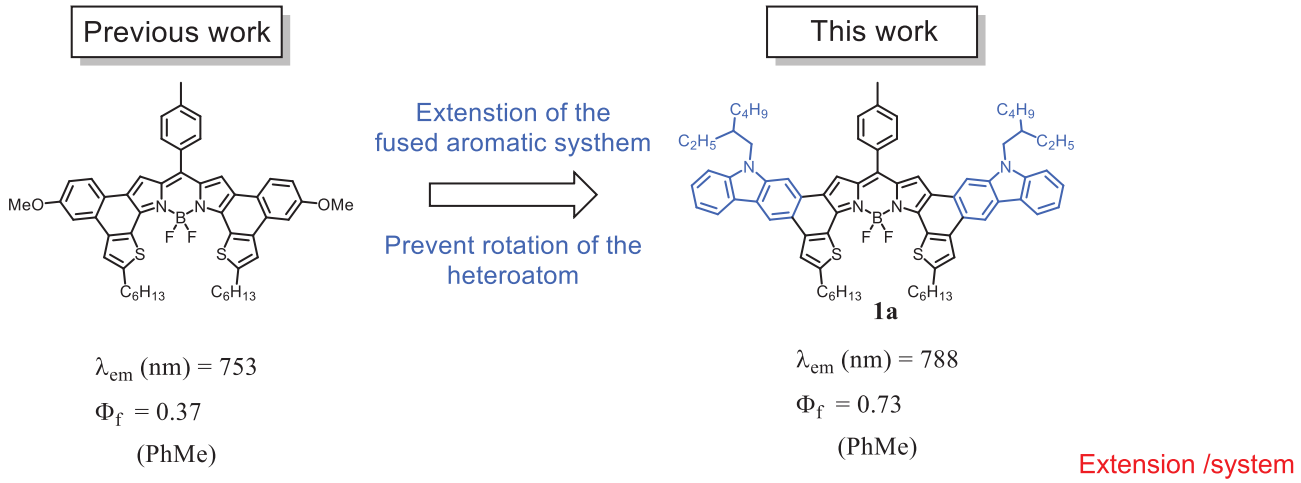

FIGURE 1 | Strategy for the improvement of NIR emission by fusion of rigidified mesomeric donor group.

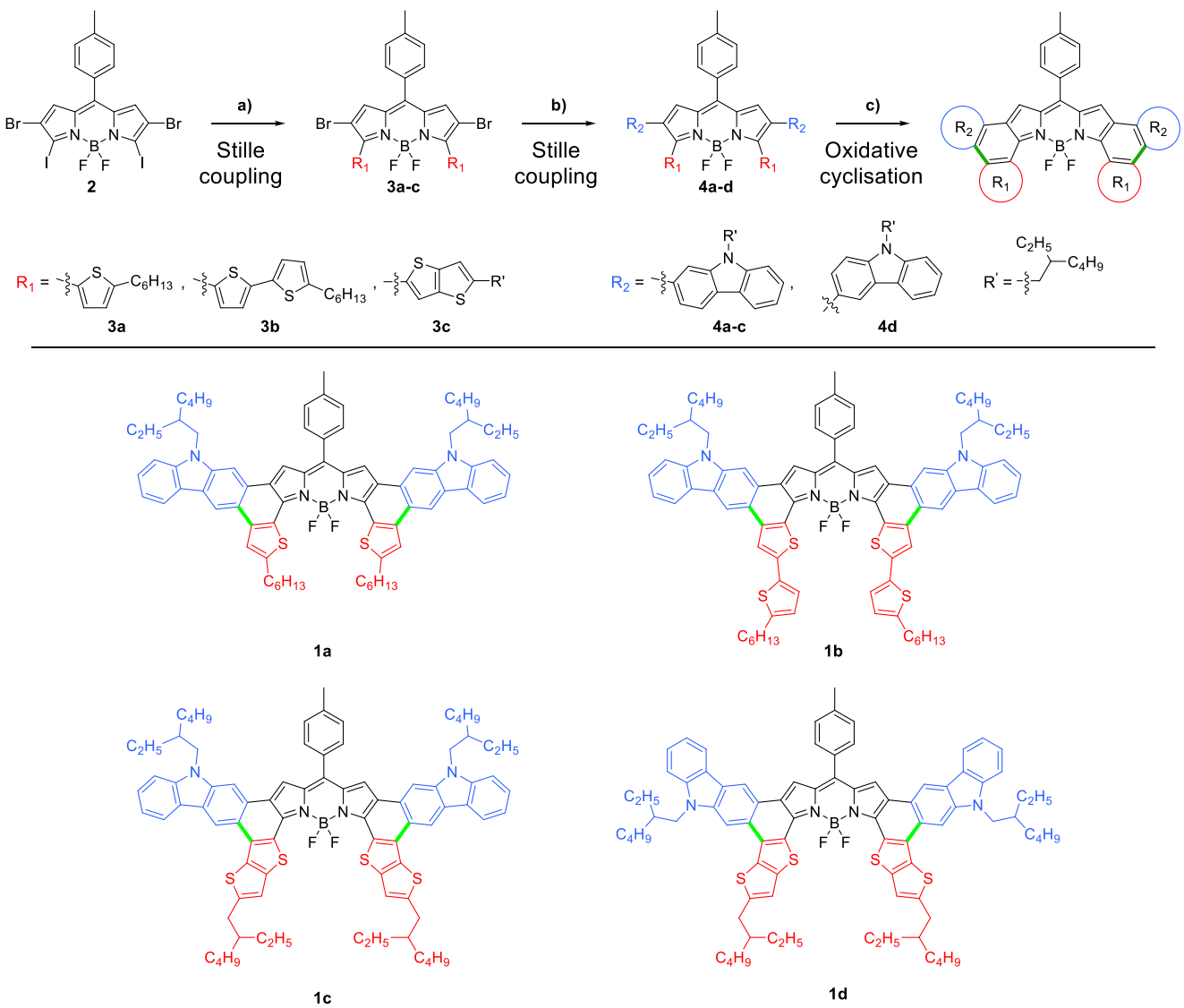

SCHEME 1 | Synthesis routes toward **1a-d**. (a) Organotin derivative, $Pd(PPh_3)_2Cl_2$, PhMe, 115°C. (b) Organotin derivative, $Pd(PPh_3)_2Cl_2$, PhMe, 115°C. (c) $AgBF_4$, $DCM/MeNO_2$, 0°C.

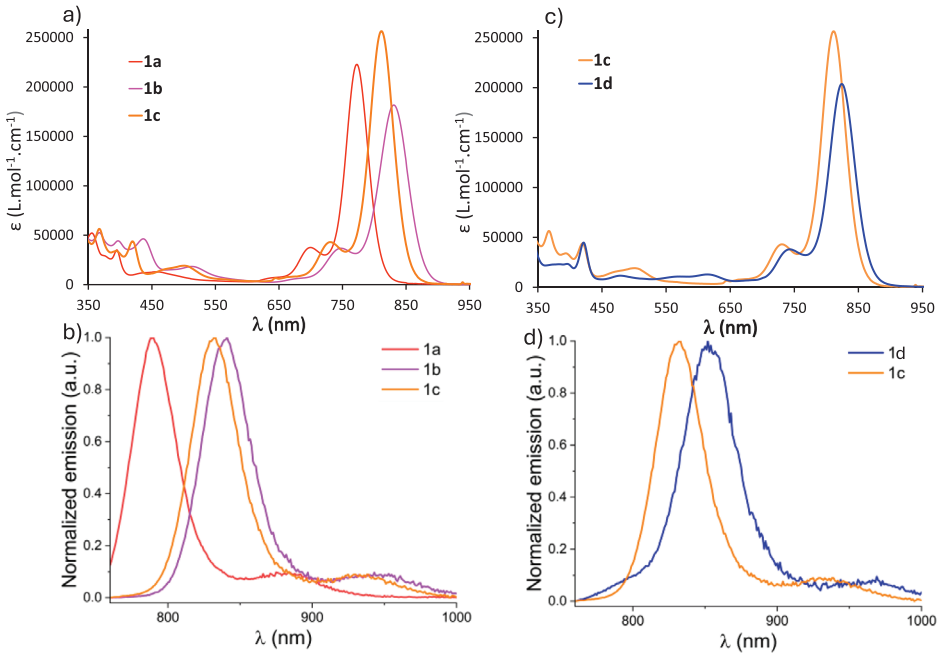

FIGURE 2 | (a) Absorption and (b) normalized emission spectra of **1a**, **1b**, and **1c** in toluene (25°C). (c) Absorption and (d) normalized emission spectra of **1c** and **1d** in toluene (25°C).

TABLE 1 | Spectroscopy data of fused BODIPY **1a-d** recorded in diluted solution at 25°C.

Cpmd	λ_{abs} (nm)	ε ($M^{-1}.cm^{-1}$)	λ_{em} [a] (nm)	Φ_f [b]	τ (ns)	k_r (10^8 cm^{-1})	k_{nr} (10^8 cm^{-1})	Δ_{SS} (cm^{-1})	Solvent
1a	772	223,000	805 (898)	0.47	3.56	1.33	1.47	531	DCM
	774	193,000	788 (860)	0.73	4.06	1.81	0.655	229	Toluene
1b	831	182,000	868 (977)	0.26	2.47	1.05	3.00	480	DCM
	832	159,000	852 (960)	0.34	2.66	1.28	2.48	297	Toluene
1c	811	256,000	839 (949)	0.37	2.83	1.31	2.39	411	DCM
	815	254,000	829 (930)	0.48	3.08	1.56	1.69	207	Toluene
1d	824	204,000	858 (970)	0.22	1.93	1.14	4.04	512	DCM
	823	218,000	837 (940)	0.33	2.60	1.27	2.58	203	Toluene

[a]Vibronic peak in bracket.
[b]Using IR125 in EtOH at 298K ($\Phi = 0.13$) as reference [35].

When the thienyl substituents at the 3,5-positions are replaced by thienothiophene and bithiophene moieties, additional redshifts of the emission are observed: 64 nm for **1b** and 41 nm for **1c** as compared to **1a** in toluene (Figure 2d). Both **1b** and **1c** also display intense NIR I emission (Φ = 0.34–0.48 in toluene). The larger shift induced by the bithiophene substituents compared to their thienothiophene counterparts can probably be attributed to a planarization of bithiophene in the excited state, inducing a larger π-conjugated system. The inversion of the orientation of the carbazole substituent (Figure 2c,d) results in a redshift of 8 nm of the emission, accompanied by a small decrease of the quantum yield ($\Phi = 0.33$ in toluene for **1d**).

In addition to their good fluorescence properties, compounds **1a–d** show a strong absorption in the NIR with molar extinction coefficients around 200 000 $M^{-1}.cm^{-1}$ which confer a very high brightness to these materials. We underline the presence of a second emission maxima for these four fused BODIPYs arises from vibronic couplings between the S_1 and S_0 states (see theory below). For compounds **1b–d** this second fluorescence peak is located at the border between NIR I and NIR II.

2.1 | X-ray Diffraction

Crystalline red plates of **1c**, grown in a mixture of acetone and dichloromethane at room temperature, were valuable enough to provide by Single Crystal x-ray Diffraction (SCXRD) analysis of the structural confirmation of the largest single BODIPY platform ever obtained by x-Ray to the best of our knowledge (Figure 3). Indeed, the longest distance between the mirrored carbons on the outer phenyl groups is ca. 23 Å. An analysis of the 37 structures of BODIPYs with symmetric peripheral fused phenyl rings found in the Cambridge Structural Database v6.00 update 08/2025 (2598

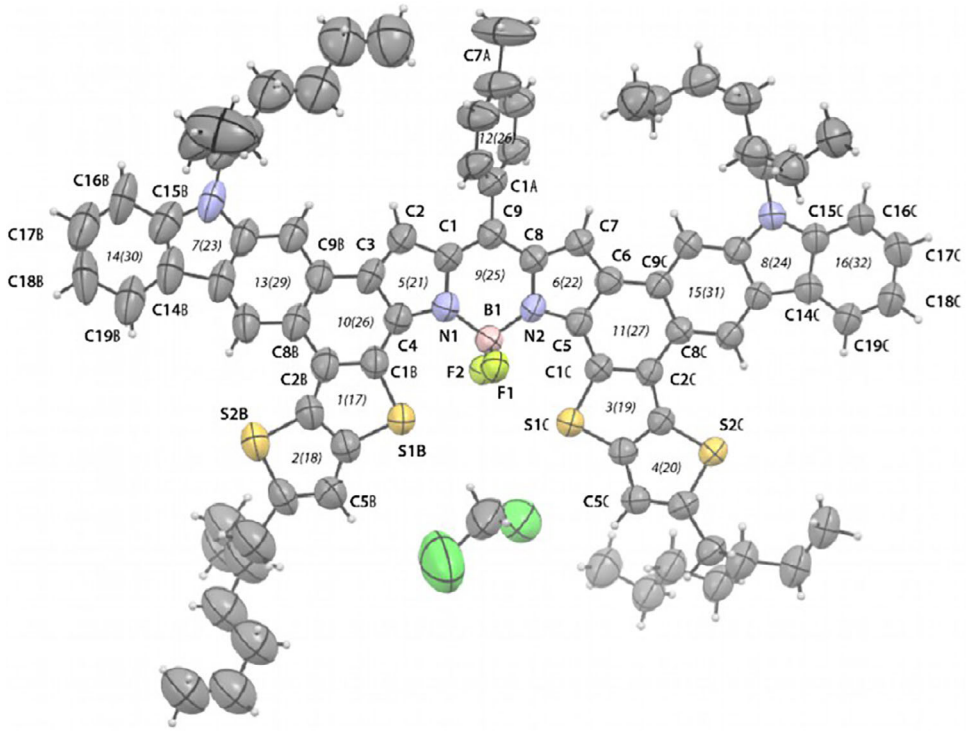

FIGURE 3 | ORTEP view of one conformer of **1c**, including a solvent dichloromethane molecule, showing the labeling schemes of atoms and planes (in italic, in brackets for the second conformer). Displacement ellipsoids are shown at the 30% probability level. H atoms are presented as small spheres of arbitrary radius. No disorder is shown for clarity. Selected geometry average parameters from table S…: <B—F> = 1.39 (2) Å; <B—N> = 1.55 (2) Å; N1(2)– C1(8) = 1.38 (1) Å; N1(2)– C4(5) = 1.37 (2) Å / < F—B—F > = 109.0(6)°; < N—B—N > = 106.8(6)°; < N—B—F > = 110.3 (10)°.

BODIPYs including 2065 F-BODIPY structures) [36] showed no larger structure.

Compound **1c** crystallized in a centrosymmetric triclinic unit cell, with two conformers essentially differing in the orientation of disordered alkyl side chains at the N1B and N1C atoms and at the extremities of the thiophene moieties. Disregarding the meso-tolyl group and the alkyl chains, **1c** exhibits an almost planar crystal structure over the fused aromatic groups around the BODIPY unit: the 52 non-hydrogen heteroatoms form a mean plane with a RMS deviation of 0.119 (resp. 0.135) Å for the two conformers present in the asymmetric unit of the crystal unit cell, for which the boron atom is off by 0.27(1) (resp. 0.29(1)) Å. The tetrahedral geometry of the boron center is observed as usual for F-BODIPYs with typical values of bond lengths and angles (see caption of Figure 3), and the strained six-membered ring chelating it through the N atoms is perpendicular to the plane of the F-B-F group. Despite the weak accuracy of our model, the other bond lengths are in the range of those for similar F-BODIPYs reported in the literature (see Table S2). The regular planarity can also be estimated from the torsion angle between the four atoms embedded in the bay regions of the BODIPY platform [−4.32/6.08° (resp. −5.25/2.62°)] (see Figures S62 and S63). This structural feature suggests an effective π-conjugation in **1a—d**. As anticipated, the *meso*-tolyl group is twisted at an angle of 56.1° (resp. 57.2°) relative to the dipyrromethene unit. Nevertheless, the orientation of the group is not constrained to be orthogonal due to the far-apart alkyl substituents or crystal packing. More details on the packing can be found in the Supporting Information (description and Figure S64)

2.2 | First-Principles Calculations

We have performed ab initio calculations to obtain insights into the photophysical properties of the new compounds. The selected theoretical protocols, as well as extra results, are given in the Supporting Information. First, to assess the quality of our theoretical estimates, we have determined the 0–0 energies of the four compounds. Our results are 1.56, 1.38, 1.45, and 1.43 eV for **1a**, **1b**, **1c**, and **1d**, respectively. These values can be directly compared to the measured absorption/fluorescence crossing points that are 1.57, 1.46, 1.50, and 1.47 eV for the same four compounds. Theory reproduces the experimental ordering, with a mean absolute error (MAE) of 0.05 eV only. This confirms the quality of the simulations. In Figures S65–S68, we report the vibrationally resolved emission spectrum determined for all compounds. As can be seen, the overall shape is nicely reproduced by theory with a very intense 0–0 peak followed by the usual vibronic contribution at lower-energy, confirming the nature of that extra peak, and that the observed emission comes, as expected, from the S_1 state.

In Figure 4, we report the electronic density difference plots. Interestingly, despite the very large size of the compounds and their near-planar pi-conjugated structures, the transition from the ground to the excited state mainly involves an electronic reorganization localized on the BODIPY core. Indeed, one notices the usual topology with a large increase of density on the *meso* carbon atom, a typical behavior of BODIPYs [37], whereas the side groups play a minor role only, though the thienyl rings at positions 3,5 play an additional donating role (blue lobes).

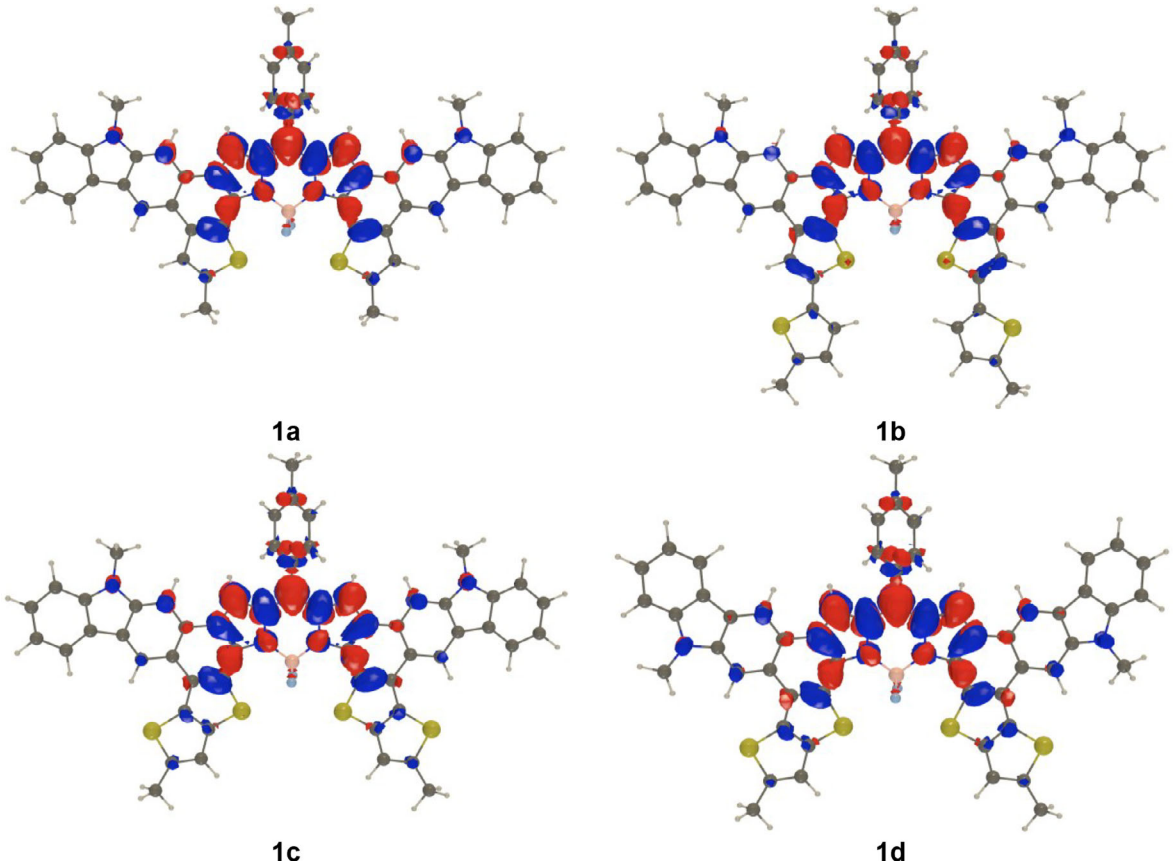

FIGURE 4 | Density difference plots for the four systems, Dr = r(S_1)-r(S_0), determined on the S_0 geometries. Navy blue and crimson red lobes indicate a decrease and an increase of electron density upon photoexcitation, respectively. Contour threshold: 8×10^{-4} au.

Let us now turn toward finding an explanation for why fluorescence is so effective in those dyes. First, the oscillator strength of the $S_1 \rightarrow S_0$ transition of these dyes is large with both TD-DFT (in DCM) and CC2 (gas phase). The large calculated values are listed in Table S5, and are at least 1.45 in TD-DFT and 1.22 in CC2, indicating very large radiative constants, k_r, and the absence of dark-state quenching. Second, the probability of intersystem-crossing (ISC) from the S_1 can be estimated by computing both the lowest singlet and triplet energies, as well as the spin-orbit couplings on the relaxed S_1 geometry. In all dyes, the T_2 state lies significantly higher than S_1, thus only the lowest triplet state is accessible for ISC. As can be seen in Table S5, rather large singlet-triplet gaps are obtained (> 0.35 eV), and the corresponding SOC matrix elements are well below 0.05 cm^{-1}, hinting at very low ISC efficiency. At this stage, we can therefore conclude that the key state is indeed S_1, that the k_r should be large, and that ISC is limited. Given that other nonradiative processes (such as electron energy transfer) are unexpected, and that the S_0-S_1 gap is small, only three relaxation pathways remain, namely fluorescence, internal conversion, and conical intersection. Due to the size of the systems, we were not able to explicitly locate the latter. However, a clue to the inaccessibility of such intersections is given by the high rigidity of the system. As shown in Figure S69, the superposed S_0 and S_1 geometries highlight *(i)* the high planarity of the systems and *(ii)* the rigidity of the geometries. Indeed, in **1a**, **1c**, and **1d**, only the methyl group in the *para*-position of the *meso*-phenyl is rotating between the two states. In **1b**, a slightly more significant modification of the geometry is visible, however such deformation remains small as compared to the size of the system. In BODIPY dyes, the accessible conical intersection is known to exhibit a large kink in the central ring along the *meso*-axis [38]. Given the size of these BODIPY dyes and the very small deformation of the relaxed excited-state geometry, we considered this deformation inaccessible.

Let us now address the simulation of the quantum yield by calculating the radiative (fluorescence) and internal conversion rates, using Fermi's Golden rule [39]. The results listed in Table S6 show radiative rates in the 1.6–2.0 x 10^8 Hz range, which are close yet slightly larger than the experimental values of Table 1, with a MAE of 0.64 x 10^8 Hz. For the internal conversion rates, theory also tends to slightly overestimate the experimental values with mean signed errors (MSE) depending on the selected broadening (see the Supporting Information for details): 3.56 x 10^8 Hz for 10 cm^{-1}, 2.00 x 10^8 Hz for 7 cm^{-1}, and 0.44 x 10^8 Hz for 5 cm^{-1}. It is satisfying that the theory provides the correct orders of magnitude. Selecting the intermediate broadening function, one computes Φ of 0.36, 0.24, 0.25, and 0.28 for **1a**, **1b**, **1c**, and **1d**, respectively. While this does not exactly follow the experimental trends, the calculations restore the correct order of magnitude, which is satisfying.

In short, theory indicates that the only two deactivation pathways are the radiative and internal conversion ones in these compounds, that is, the two always existing pathways. Given that these systems present very large ε, this hints that further

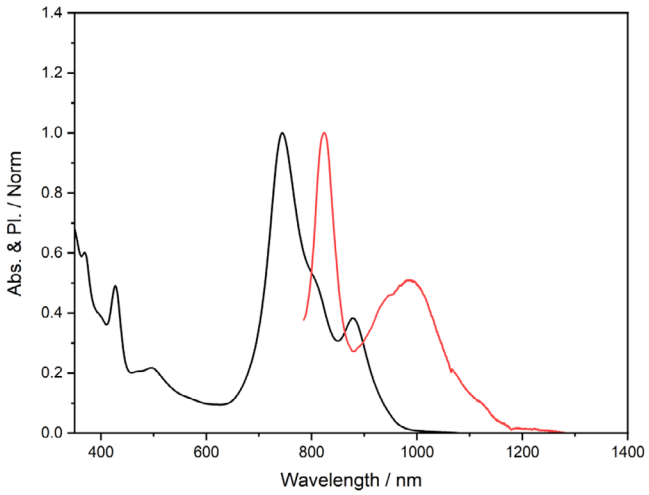

FIGURE 5 | Absorption (black line) and emission (red line) spectra of **1c**@F127-SiO_2 NPs.

increasing their brightness is likely challenging, since there is no obvious detrimental deactivation route to be suppressed.

2.3 | Nanoparticles Loadings and Properties

To validate a practical application in imaging, compound **1c**, which exhibits the best compromise in Φ and λ_{em}, was selected for encapsulation in a silica-stabilized pluronic F127 micelle (1c@F-127-SiO_2 NPs). This type of NPs, which are easy to obtain, are known to retain the optical properties of organic fluorophores observed in apolar media for dyes insoluble in water [40]. Dynamic light scattering (DLS) measurement indicates an average hydrodynamic size of 29 nm in saline medium (9 g/L NaCl in water), typical of such fluorophores (Figure S70) [41]. The absorption and emission spectra of 1c@F127-SiO_2 are given in Figure 6. The absorption spectrum shows two clear peaks in the low energy area, one at 755 nm hypsochromically shifted compared to the S_0-S_1 transition in toluene, and a second at 890 nm bathochromically shifted compared to toluene. Due to the planar nature of **1c,** these two peaks could be attributed respectively to the formation of H- and J- aggregates inside the NP. The small shoulder observed at 820 nm likely originates from non-aggregate dyes. Interestingly, a significant amount of fluorophore organized as J-aggregates displays an emission maximum at 927 nm with an intense shoulder at 1035 nm (Figure 5). This efficient emission (NPs $\Phi = 0.004$) in the NIR-II region of these water-soluble NPs led us to test its effectiveness in microscopy.

3 | NIR-II Noninvasive Imaging in Mice

The behavior of the BODIPY **1c** encapsulated in the NP formulation, that is, **1c**@F127-SiO_2 NPs, was investigated in mice bearing subcutaneous U-87 MG tumor (Figure 6). The rodents were injected with 200 µL of 1 µM dye solution, that is, 0.2 nmol of BODIPY **1c** per mouse, corresponding to a low fluorophore dose. The NIR-II fluorescence was recorded from 1064 to 1700 nm after an excitation at 808 nm. The NPs circulate in the mouse's body and show an accumulation in the liver and the spleen, characteristic of the elimination of NPs with similar hydrodynamic size. The fluorescent NPs are observed in the tumor, with a better contrast at 24 h and 48 h post injection. The tumor-to-surrounding tissue ratio increases in a time-dependent manner, reaching 2 in 24 h–48 h. However, the ex vivo ratio between tumor and muscle reaches 4 at these time-points. Notably, no unexpected accumulation was seen. Such ratios hint at a high tumor specificity, according to the Rose criterion [42]. The tumor accumulation is higher than in most of the organs as indicated in the Figure 6a; the accumulation of the **1c**@F127-SiO_2 NPs in the skin prevented to clearly observed the tumor area.

While the injected dose here is 0.2 nmol, the conventional dose of fluorescent probe for in vivo imaging is between 1–10 nmol of dye, and can even increase to 25–40 nmol for BODIPY derivatives [43, 44]. in the absence of specific bioconjugation (i.e., antibodies), confirming the interest of our dyes [45, 46]. The strong increase in fluorescent signal observed in the liver between 4 h and 24 h leads to a saturated and persistent signal in this area until 48 h. Several compounds of the BODIPY family have been reported to exhibit comparable or even lower in vivo imaging performance [30]. Whilst strict comparison of imaging results across different studies is known to be challenging due to experimental setups (e.g., excitation sources, detection systems, filter sets, acquisition parameters, and image processing methods), comparisons can be made with one previous work [30]. We found that dye **1c** delivers similar-to-higher fluorescence for liver, the main organ of accumulation of both compounds.

4 | Conclusions

We reported the original synthesis and outstanding emissive properties of fused extended BODIPY dyes bearing carbazole derivatives on the 2,6 positions and various thienyl donor groups on the 3,5 positions. The synthesis starts from 2,6-dibromo-3,5-diiodo-BODIPY, allowing efficient successive Stille cross-coupling reactions. A synthetic breakthrough comes from the use of a silver(I) salt as oxidant for the last cyclization step, allowing reaching very good yields and no parasitical chlorination, in contrast to the classical $FeCl_3$ oxidative process. The new compounds exhibit record brightness for fluorophores in this region of the radiative spectrum (emission in the 800–850 nm range), thanks to an intense absorption coefficient ($1.8–2.5.10^5$ M^{-1} cm^{-1}) and large quantum yield (up to 73%). Theoretical calculations indicate that these dyes are not prone to intersystem crossing, possess larger oscillator strengths, and have quasi-equivalent ground and excited-state geometries, all aspects being favorable for achieving the observed high quantum yields. Importantly, the only nonradiative pathway that appears open is the internal conversion one; this path is related to the nonadiabatic couplings between the two states and can hardly be suppressed. Despite the poor water solubility of these prototypical molecules, we were able to encapsulate them in water-soluble silica-based NPs and maintain a significant emission. Taking advantage of the strong emission of J-aggregates with a peak at 925 nm and a broad 975–1150 nm shoulder, these particles were successfully used in NIR-II noninvasive imaging experiments in mice. The very low injected dose of 0.2 nmol allowed the detection of the tumor. The nanoformulation distributed very well in the bloodstream though, he uptake in the skin was not negligible, which reduced the contrast while the tumor-to-muscle ratios were higher than

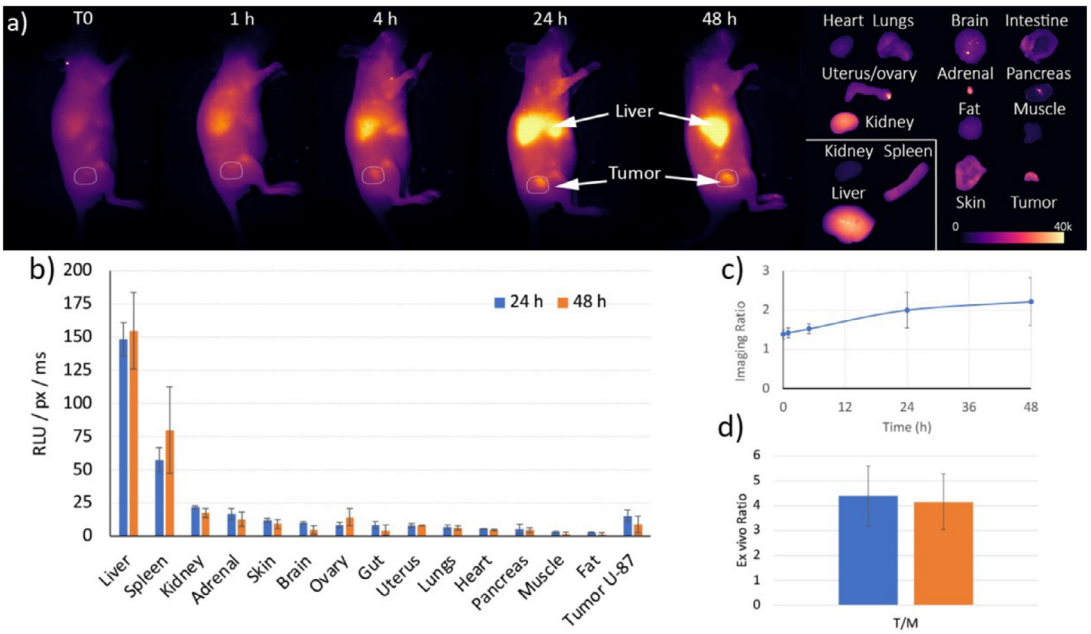

FIGURE 6 | In vivo behavior of the NPs loaded with 1c (1c@F127-SiO_2 NPs). (a) Representative examples of U-87 MG bearing mice injected with the nanoparticles loaded with 1c@F127-SiO_2 NPs before, and 1 h, 4 h, 24 h, and 48 h after intravenous injection. The noninvasive images indicated an uptake in the liver and a time-dependent accumulation in the tumor, surrounded by a dashed-line. The fluorescent signal of organs collected at 48 h is shown (collection of the signal: 1000 ms). The signal of the kidney, spleen, and liver (bottom left) was 200 ms. (b) Ex vivo quantification of the fluorescence signal in the different organs and the tumor, 24 h and 48 h after injection ($n = 3$ / per condition). The in vivo (c) and ex vivo (d) tumor/adjacent tissue ratios are indicated. Results are expressed as mean ± standard deviation.

4. Such ratios hint at a high tumor specificity, according to the Rose criterion. These very promising results pave the way to further developments of these new BODIPY derivatives for biological applications, for example, in real-time image-guided surgery and preclinical imaging. To this end, the next steps consist of adapting this family of compounds to the deep NIR by further redshifting their optical spectra, and concomitantly introducing specific functions to enhance water compatibility and bioconjugation strategies.

Acknowledgments

F.C. is grateful to the University of Strasbourg for "*contrat doctoral d'établissement*." The authors are deeply thankful to Agence Nationale de la Recherche for the financial support of this project ANR-23-CE07-0027-01 (ULBONIR). This research used resources of the GLiCID Computing Facility (Ligerien Group for Intensive Distributed Computing, 10.60487/glicid, Pays de la Loire, France). We acknowledge the use of the synchrotron-radiation facility at the SOLEIL synchrotron, Gif-sur-Yvette, France, under the BAG proposal 20191181. We thank Dr. Pierre Legrand and the staff of the PROXIMA-1 beamline at SOLEIL for full assistance with data collection, especially in that difficult context. We thank the Optimal imaging small animal platform, a platform supported by France Life Imaging (French program "Investissement d'Avenir" grant; "Infrastructure d'avenir en Biologie Santé," ANR-11-INBS-0006) and the IBISA French consortium "Infrastructures en Biologie Santé et Agronomie".

Open access publication funding provided by COUPERIN CY26.

Conflicts of Interest

The authors declare no conflicts of interest.

Data Availability Statement

The data that support the findings of this study are available in the supporting information of this article.

References

1. I. Johnson, ed., *The Molecular Probes Handbook: A Guide to Fluorescent Probes and Labeling Technologies* (Life Technologies Corp, 2010).

2. C. Li, G. Chen, Y. Zhang, F. Wu, and Q. Wang, "Advanced Fluorescence Imaging Technology in the Near-Infrared-II Window for Biomedical Applications," *Journal of the American Chemical Society* 142 (2020): 14789–14804, https://doi.org/10.1021/jacs.0c07022.

3. S. Zhu, R. Tian, A. L. Antaris, X. Chen, and H. Dai, "Near-Infrared-II Molecular Dyes for Cancer Imaging and Surgery," *Advanced Materials* 31 (2019): 1900321, https://doi.org/10.1002/adma.201900321.

4. K. Lee, H.-D. Um, D. Choi, et al., "The Development of Transparent Photovoltaics," *Cell Reports Physical Science* 1 (2020): 100143.

5. F. Grifoni, M. Bonomo, W. Naim, et al., "Toward Sustainable, Colorless, and Transparent Photovoltaics: State of the Art and Perspectives for the Development of Selective Near-Infrared Dye-Sensitized Solar Cells," *Advanced Energy Materials* 11 (2021): 2101598, https://doi.org/10.1002/aenm.202101598.

6. M. Liu, J. Wang, Z. Zhao, et al., "Ultra-Narrow-Band NIR Photomultiplication Organic Photodetectors Based on Charge Injection Narrowing," *Journal of Physical Chemistry Letters* 12, no. 11 (2021): 2937–2943.

7. S. He, J. Song, J. Qu, and Z. Cheng, "Crucial Breakthrough of Second Near-Infrared Biological Window Fluorophores: Design and Synthesis Toward Multimodal Imaging and Theranostics," *Chemical Society Reviews* 47 (2018): 4258–4278, https://doi.org/10.1039/c8cs00234g.

8. S. Pascal, S. Denis-Quanquin, F. Appaix, et al., "Keto-Polymethines: A Versatile Class of Dyes With Outstanding Spectroscopic Properties for in Cellulo and in Vivo Two-Photon Microscopy Imaging," *Chemical Science* 8 (2017): 381–394, https://doi.org/10.1039/c6sc02488b.

9. E. D. Cosco, J. R. Caram, O. T. Bruns, et al., "Flavylium Polymethine Fluorophores for Near- and Shortwave Infrared Imaging," *Angewandte Chemie International Edition* 56 (2017): 13126–13129, https://doi.org/10.1002/anie.201706974.

10. H. C. Friedman, E. D. Cosco, T. L. Atallah, S. Jia, and E. M. Slette, "Establishing Design Principles for Emissive Organic SWIR Chromophores From Energy Gap Laws," *Chem* 7 (2021): 3359–3376, https://doi.org/10.1016/j.chempr.2021.09.001.

11. D. Liu, Z. He, Y. Zhao, et al., "Xanthene-Based NIR-II Dyes for in Vivo Dynamic Imaging of Blood Circulation," *Journal of the American Chemical Society* 143 (2021): 1713, https://doi.org/10.1021/jacs.1c07711.

12. E. Cosco, A. L. Spearman, S. Ramakrishnan, et al., "Shortwave Infrared Polymethine Fluorophores Matched to Excitation Lasers Enable Non-Invasive, Multicolour in Vivo Imaging in Real Time," *Nature Chemistry* 12 (2020): 1123–1130, https://doi.org/10.1038/s41557-020-00554-5.

13. E. Cosco, B. A. Arús, A. L. Spearman, et al., "Bright Chromenylium Polymethine Dyes Enable Fast, Four-Color in Vivo Imaging With Shortwave Infrared Detection," *Journal of the American Chemical Society* 143 (2021): 6836–6846, https://doi.org/10.1021/jacs.0c11599.

14. Y.-F. Ou, T.-B. Ren, L. Yuan, and X.-B. Zhang Chem, "Molecular Design of NIR-II Polymethine Fluorophores for Bioimaging and Biosensing," *Biomed Imaging* 1 (2023): 220–233, https://doi.org/10.1021/cbmi.3c00040.

15. Y. Liu, S. K. Li, Y. Sun, et al., "Versatile Types of Inorganic/Organic NIR-IIa/IIb Fluorophores: From Strategic Design Toward Molecular Imaging and Theranostics," *Chemical Reviews* 122 (2021): 209, https://doi.org/10.1021/acs.chemrev.1c00553.

16. A. L. Antaris, H. Chen, K. Cheng, et al., "A Small-Molecule Dye for NIR-II Imaging," *Nature Materials* 15 (2016): 235–242, https://doi.org/10.1038/NMAT4476.

17. X. Zhao, F. Zhang, and Z. Lei, "The Pursuit of Polymethine Fluorophores With NIR-II Emission and High Brightness for in Vivo Applications," *Chemical Science* 13 (2022): 11280–11293, https://doi.org/10.1039/D2SC03136A.

18. J. A. Carr, D. Franke, J. R. Caram, et al., "Shortwave Infrared Fluorescence Imaging With the Clinically Approved Near-Infrared Dye Indocyanine Green," *Proceedings of the National Academy of Sciences USA* 115 (2018): 4465, https://doi.org/10.1073/pnas.1717917115.

19. G. Deng, S. Zhang, X. Peng, et al., "Methylene Blue: An FDA-Approved NIR-II Fluorogenic Probe With Extremely low pH Responsibility for Hyperchlorhydria Imaging," *Chemical & Biomedical Imaging* 2, no. 10 (2024): 683–688, https://doi.org/10.1021/cbmi.4c00011.

20. C. Li, W. Li, H. Liu, Y. Zhang, G. Chen, Z. Li, and Q. Wang, "An Activatable NIR-II Nanoprobe for in Vivo Early Real-Time Diagnosis of Traumatic Brain Injury," *Angewandte Chemie International Edition* 59 (2020): 247, https://doi.org/10.1002/anie.201911803.

21. G. Hong, J. C. Lee, J. T. Robinson, et al., "Multifunctional in Vivo Vascular Imaging Using Near-Infrared II Fluorescence," *Nature Medicine* 18 (2012): 1841–1846, https://doi.org/10.1038/nm.2995.

22. D. Tang, Y. Yu, J. Zhang, X. Dong, C. Liu, and H. Xiao, "Self-Sacrificially Degradable Pseudo-Semiconducting Polymer Nanoparticles That Integrate NIR-II Fluorescence Bioimaging, Photodynamic Immunotherapy, and Photo-Activated Chemotherapy," *Advanced Materials* 34 (2022): 2203820, https://doi.org/10.1002/adma.202203820.

23. W. Xu, D. Wang, and B. Z. Tang, "NIR-II AIEgens: A Win–Win Integration Towards Bioapplications," *Angewandte Chemie International Edition* 60 (2021): 7476, https://doi.org/10.1002/anie.202005899.

24. Z. Lei and F. Zhang, "Molecular Engineering of NIR-II Fluorophores for Improved Biomedical Detection," *Angewandte Chemie International Edition* 60 (2021): 16294–16308, https://doi.org/10.1002/anie.202007040.

25. T. Kowada, H. Maeda, and K. KikuchiChem, "BODIPY-Based Probes for the Fluorescence Imaging of Biomolecules in Living Cells," *Chemical Society Reviews* 44 (2015): 4953–4972, https://doi.org/10.1039/C5CS00030K.

26. Q. Wu, Q. G. Kang, X. Guo, et al., "Strategic Construction of Ethene-Bridged BODIPY Arrays With Absorption Bands Reaching the Near-Infrared II Region," *Organic Letters* 22 (2020): 7513, https://doi.org/10.1021/acs.orglett.0c02704.

27. L. Bai, P. Sun, Y. Liu, H. Zhang, et al., "Novel aza-BODIPY Based Small Molecular NIR-II Fluorophores for in Vivo Imaging," *Chemical Communications* 55 (2019): 10920, https://doi.org/10.1039/C9CC03378E.

28. M. Bendellaa, C. Cave, A. Godard, et al., "WazaGaY: An Innovative Aza-BODIPY-Derived Near-Infrared Fluorescent Probe for Enhanced Tumor Imaging," *Journal of Medicinal Chemistry* 67 (2024): 16635–16648, https://doi.org/10.1021/acs.jmedchem.4c01435.

29. J. Pliquett, A. Dubois, C. Racoeur, et al., "A Promising Family of Fluorescent Water-Soluble Aza-BODIPY Dyes for in Vivo Molecular Imaging," *Bioconjugate Chemistry* 30 (2019): 1061–1066, https://doi.org/10.1021/acs.bioconjchem.8b00795.

30. A. Godard, G. Kalot, J. Pliquett, et al., "Water-Soluble Aza-BODIPYs: Biocompatible Organic Dyes for High Contrast in Vivo NIR-II Imaging," *Bioconjugate Chemistry* 31 (2020): 1088–1092, https://doi.org/10.1021/acs.bioconjchem.0c00175.

31. G. Xu, Q. Yan, X. Lv, Y. Zhu, et al., "Imaging of Colorectal Cancers Using Activatable Nanoprobes With Second Near-Infrared Window Emission," *Angewandte Chemie International Edition* 57 (2018): 3626, https://doi.org/10.1002/anie.201712528.

32. F. Ceugniet, Q. Huaulmé, A. Sutter, D. Jacquemin, N. Leclerc, and G. Ulrich, "Hetero-Substituted Aβ-Fused BODIPY," *Chemistry – A European Journal* 28 (2022): e202200130, https://doi.org/10.1002/chem.202200130.

33. Q. Huaulmé, A. Sutter, S. Fall, et al., "Versatile Synthesis of α-fused BODIPY Displaying Intense Absorption in the NIR Region and High Electron Affinity," *Journal of Materials Chemistry C* 6 (2018): 9925–9931, https://doi.org/10.1039/C8TC03138J.

34. J. Wu, M. D. Watson, L. Zhang, Z. Wang, and K. Müllen, "Hexakis(4-iodophenyl)- Peri -Hexabenzocoronene- A Versatile Building Block for Highly Ordered Discotic Liquid Crystalline Materials," *Journal of the American Chemical Society* 126 (2004): 177–186, https://doi.org/10.1021/ja037519q.

35. K. Rurack and M. Spieles, "Fluorescence Quantum Yields of a Series of Red and Near-Infrared Dyes Emitting at 600–1000 Nm," *Analytical Chemistry* 83 (2011): 1232–1242, https://doi.org/10.1021/ac101329h.

36. C. R. Groom and F. H. Allen, "The Cambridge Structural Database in Retrospect and Prospect," *Angewandte Chemie International Edition* 53 (2014): 662–671, https://doi.org/10.1002/anie.201306438.

37. B. Le Guennic and D. Jacquemin, "Taking up the Cyanine Challenge With Quantum Tools," *Accounts of Chemical Research* 48 (2015): 530–537, https://doi.org/10.1021/ar500447q.

38. A. Prlj, L. Vannay, and C. Corminboeuf, "Fluorescence Quenching in BODIPY Dyes: The Role of Intramolecular Interactions and Charge Transfer," *Helvetica Chimica Acta* 100 (2017): e1700093, https://doi.org/10.1002/hlca.201700093.

39. M. T. do Casal, K. Veys, M. H. E. Bousquet, D. Escudero, and D. Jacquemin, "First-Principles Calculations of Excited-State Decay Rate Constants in Organic Fluorophores," *Journal of Physical Chemistry A* 127 (2023): 10033–10053, https://doi.org/10.1021/acs.jpca.3c06191.

40. E. Rampazzo, S. Bonacchi, D. Genovese, et al., "Pluronic-Silica (PluS) Nanoparticles Doped With Multiple Dyes Featuring Complete Energy Transfer," *Journal of Physical Chemistry C* 118 (2014): 9261–9267, https://doi.org/10.1021/jp501345f.

41. Z. Zheng, F. Caraguel, Y.-Y. Liao, C. Andraud, B. van der Sanden, and Y. Bretonnière, "Photostable Far-Red Emitting Pluronic Silicate Nanoparticles: Perfect Blood Pool Fluorophores for Biphotonic in Vivo Imaging of the Leaky Tumour Vasculature," *RSC Advances* 6 (2016): 94200–94205.

42. J. T. Bushberg, J. A. Seibert, E. M. L. Jr, and J. M. Boone, *The Essential Physics of Medical Imaging*, Third Edition, (Lippincott Williams & Wilkins, 2011).

43. B. Rong, X. Dong, and W. Zhao, "Synthesis and Evaluation of a Novel BODIPY Fluorescent Probe Targeting Integrin $\alpha_v\beta_3$ for Cancer Diagnosis," *European Journal of Medicinal Chemistry* 282 (2025): 117056, https://doi.org/10.1016/j.ejmech.2024.117056.

44. A. Godard, G. Kalot, M. Privat, et al., "NIR-II aza-BODIPY dyes Bioconjugated to Monoclonal Antibody Trastuzumab for Selective Imaging of HER2-Positive Ovarian Cancer," *Journal of Medicinal Chemistry* 66 (2023): 5185–5195.

45. L. Sancey, S. Dufort, V. Josserand, et al., "Drug Development in Oncology Assisted by Noninvasive Optical Imaging," *JL Coll, Int J Pharm* 379 (2009): 309–316, https://doi.org/10.1016/j.ijpharm.2009.05.034.

46. F. D. Nascimento, L. Sancey, A. Pereira, et al., "The Natural Cell-Penetrating Peptide Crotamine Targets Tumor Tissue in Vivo and Triggers a Lethal Calcium-Dependent Pathway in Cultured Cells," *Molecular Pharmaceutics* 9 (2012): 211–221, https://doi.org/10.1021/mp2000605.

Supporting Information

Additional supporting information can be found online in the Supporting Information section.

Supporting File 1: The authors have cited additional references within the Supporting Information.

Supporting File 2: anie71753-sup-0002-Data.zip.